ORIGINAL ARTICLE

Microstructure and mechanical properties of CuZn-Al$_2$O$_3$ nanocomposites produced by friction stir processing

Akbar Heidarzadeh[1] · Babak Taghizadeh[2] · Ahad Mohammadzadeh[2]

Abstract

For the first time, ceramic nano particles were incorporated into the brass alloy to produce surface nano composites by friction stir processing. For this aim, Al$_2$O$_3$ particles with an average diameter of 30 nm were inserted into a Cu-37Zn alloy at different tool rotational speeds of 450, 710, and 1120 rpm, multi passes, and a constant traverse speed of 100 mm/min. The microstructures of the processed materials were analyzed using optical and scanning electron microscopes equipped with an energy dispersive spectroscopy. In addition, tensile test was employed to evaluate the mechanical properties. The results showed that the optimum rotational speed was 710 rpm. At lower rotational speeds, Al$_2$O$_3$ particles were agglomerated. On the other hand, at higher rotational speeds, tool was damaged by severe wear. The effect of multi passes showed that one and two passes could not distribute the Al$_2$O$_3$ particles, uniformly. However, three passes resulted in a uniform distribution of the Al$_2$O$_3$ particles inside a bimodal grain structure composed of both 3–5 μm grains and ultra-fine grains (< 1 μm). By using multi-pass friction stir processing, a synergic increase in ultimate tensile strength and elongation was obtained. Moreover, three passes caused superior mechanical properties i.e. ultimate tensile strength of 430 MPa and elongation of 39%. The fracture behavior and strengthening mechanisms are also discussed in details.

Keywords Ceramic nanoparticles · Al$_2$O$_3$ · Brass · Friction stir processing · Microstructure · Mechanical properties

1 Introduction

Composite structures due to their unique characteristics such as a very good combination of strength and ductility have attracted the attention of researchers in both academic and industrial areas. One of the interesting composite structures is metal matrix composites (MMCs) reinforced with ceramic particles. In fact, the incorporation of ceramic particles into the metals covers their disadvantages such as low hardness, strength and wear resistance. In this regard, lots of investigations have been undertaken to develop different methods for production of metal-ceramic composite structures [1].

The conventional methods for production of MMCs are liquid state techniques, in which the ceramic particles insert into the molten metal. Thus, these types of composites have a casting structure, which contains dendrites, segregation of alloying elements and ceramic particles, porosities, shrinkages and etc. In addition, the non-wettability of ceramic particles by molten metals is another difficulty during liquid state methods, which does allow the ceramic phases to incorporate into the molten matrix. Moreover, the chemical reaction between ceramic particle and molten metal causes formation of brittle phases, which results in lower ductility. Fortunately, solid state methods overcome these difficulties [2].

Friction stir processing (FSP) as a new solid state route for production of surface composites has been proved to be applicable for a wide range of metals and alloys. It is based on friction stir welding (FSW) method. In this method, a non-consumable rotating tool inserts into the materials and then traverses along the process line. The friction between tool and materials causes increase of temperature, however, the material does not melt. On the other hand, rotating tool result in severe plastic deformation (SPD) of the material.

✉ Akbar Heidarzadeh
ak.hz62@gmail.com; ac.heydarzadeh@azaruniv.ac.ir

✉ Ahad Mohammadzadeh
amzadeh@ymail.com; amohammadzadeh@maragheh.ac.ir

[1] Department of Materials Engineering, Azarbaijan Shahid Madani University, P.O.Box: 53714-161, Tabriz, Iran

[2] Department of Materials Engineering, Faculty of Engineering, University of Maragheh, P.O.Box: 83111-55181, Maragheh, Iran

Thus, the presence of both the deformation and temperature leads to occurrence of dynamic restoration mechanisms such as dynamic recrystallization (DRX), and hence it causes formation of fine and equiaxed grains congaing high density of dislocations [3].

FSP can be used for two main aims. The first aim is a microstructural modification in which the initial structure of the material is replaced with new one. For example, in the case of cast structures, FSP eliminates the dendrites, porosities and segregations, and it generates sound materials with fine equiaxed grains that increases the mechanical responses of the materials [4, 5]. Kumar et al. [4] applied FSP to graphene nanoplatelets (GNPs) physically compacted on the surface of squeeze cast A356 alloy to incorporate GNPs within the matrix and to improve its mechanical properties. Their results showed that squeeze casting resulted in finer size silicon and intermetallic compounds in cast microstructure, and subsequently FSP further refined the microstructure of squeeze cast A356 alloy, and GNP reinforced A356 alloy. Yao et al. [5] successfully fiction stir processed the ductile cast iron at a tool rotational rate of 1000 rpm and a traveling speed of 90 mm/min, and an obvious defect-free processed zone was obtained. Their results showed that the high density of ultra-refined and nearly equiaxed graphite particles (0.5–1 μm) uniformly were distributed in most parts of the stir zone. The second aim is production of MMCs reinforced with ceramic particles. For this purpose, some steps are added to the conventional FSP. Usually, a groove or some holes are machined on the surface of the base metals (BMs), and they are filled with ceramic nano particles before FSP. Then, FSP distributes the ceramic particles into the BMs and generates composite structures [6–8]. Lee et al. [6] applied FSP to incorporate 5–10 vol.% nano-sized SiO2 into an AZ61Mg alloy matrix to form bulk composites. The nano-particles were uniformly dispersed after four FSP passes, and the average grain sizes of the composites varied within 0.5–2 μm. Ahmadkhaniha et al. [7] produced composite layers containing ~ 0.8%vol Al_2O_3 nanoparticles were produced on AZ91 magnesium alloy by FSP. Their results showed that the presence of nano Al_2O_3 reduced the grain sizes of the layers further and increased their hardness. Du et al. [8] has successfully fabricated a $Al–Al_2O_3$–CNTs composite using FSP. Their results disclosed that uniform dispersion of nano-particles in the metal matrix was observed. In addition, significant improvement in the micro-hardness and tensile strengths were obtained through the addition of nano particles.

In recent years, some investigators have tried to produce MMCs reinforced with ceramic nanoparticles using FSP [9–11]. For example, Heidarzadeh et al. [9] fabricated $Cu-Al_2O_3$ nanocomposite using FSP and they studied the microstructural evolution by orientation imaging microscopy (OIM). They reported that the presence of Al_2O_3 nano-particles during FSP causes formation of ultra-fine grained (UFG) structure with an average grain size of 0.7 μm. Shafiei-Zarghani et al. [10] studied the microstructure and mechanical properties of $Al-Al_2O_3$ nanocomposite produced by FSP. They have shown that by increasing the number of FSP passes, the distribution of the nano particles in the matrix is more uniform, and the hardness and wear resistance of the composites increase. Khodabakhshi et al. [11] fabricated Al–Mg alloy matrix composites reinforced with graphene nano-platelets (GNPs) using multi-pass FSP. They showed that multi-pass FSP causes a uniform distribution of GNPs in a recrystallized matrix with an average grain size of 2.1 μm. They also confirmed that hardness increases by 53% in comparison with that of the base material.

FSW of brass (Cu–Zn) alloys have attracted the attention of researchers in recent years because of the fusion welding difficulties. However, FSP of brass alloys has not been yet reported. Therefore, the aim of this study was to fabricate the brass nanocomposites using FSP. For this purpose, the FSP was performed at different conditions and the microstructure and mechanical properties so of the processed materials have been investigated.

2 Materials and methods

Brass (Cu-30Zn) plates were the base materials (BMs), which had a size of 100 mm × 100 mm × 2 mm in length, width, and thickness, respectively. The tool with its dimensions used for FSP is shown in Fig. 1, which was made of H13 tool steel. The diameter of the tool shoulder, the diameter of the tool pin, and the length of the tool pin were 12, 3, and 1.75 mm, correspondingly. Prior to FSP, grooves with a width of 1 mm and a depth of 1.5 mm were machined on the surface of brass plates. Then, the Al_2O_3 nanoparticles (with an average diameter of 30 nm) were impacted into the groves. The FSP was conducted in two separated steps. First, a rotating pin less tool was used to close the surface of the grooves, which causes encapsulation of nanoparticles. Secondly, a tool consisting of both the pin and shoulder was inserted into the material, and then traverse along the processing line. The FSP was conducted at different tool rotational speeds of 450, 710, and 1120 rpm at constant traverse speed of 100 mm/min. The concept of heat input explained by other researchers [12–14] was used, qualitatively. In summary, higher rotational speeds and lower traverse speeds results in more heat input during FSP [12–14]. After optimizing the tool rotational speed based on the macro-structural and microstructural characteristics, multi-pass FSP was done for different number of passes i.e. 1–3 passes. In all experiments, the angle between the tool axis and normal direction of the plate's surface was kept constant at 3 degrees.

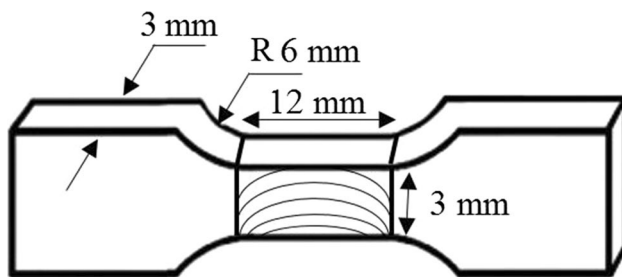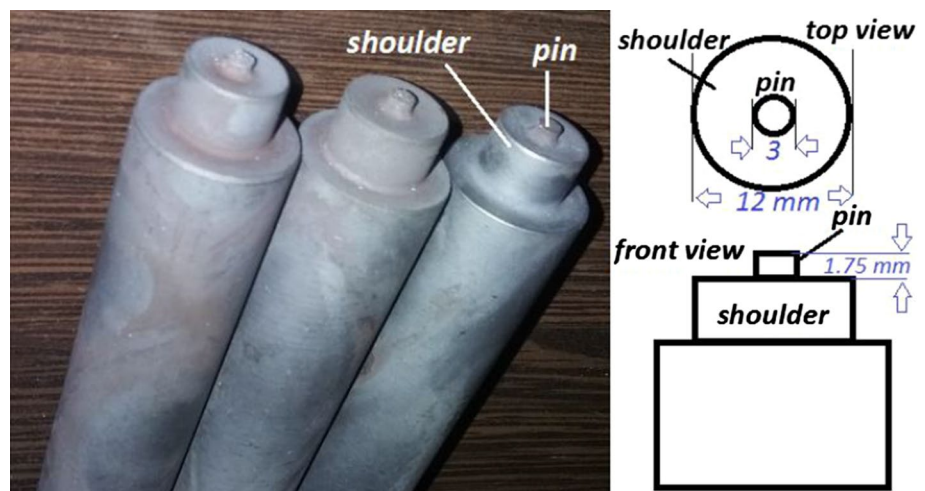**Fig. 1** FSP tools used in this study

Fig. 2 Schematic of tensile test sample with its corresponding dimensions

The microstructure of the joints was first examined by using an optical microscopy (OM). The OM specimens were cross sectioned from the joints perpendicular to the FSW direction, and they were then prepared by mechanical polishing and etching with a solution of 50 mL HCl, 10 mL H_2O and 5 g FeCl3. A Philips XL30 E-SEM field emission gun scanning electron microscope was employed. The linear intercept method was employed for grain size measurements, and the annealing twins were not considered as grains. Three longitudinal tensile test samples per condition were wire cut from the joints along the welding line, according to the dimensions in Fig. 2. Tensile tests were conducted using a universal tensile test machine (model: TB10T) at a crosshead speed of 1 mm/min. The tensile tests were all conducted at room temperature.

3 Results and discussion

3.1 Microstructural evolution

The macrostructure of the friction stir processed materials were composed of three different areas including BM, thermomechanically affected zone (TMAZ), and stir zone (SZ). It is notable that the heat affected zone (HAZ) was not seen in the macrostructures, which may be due to low heat input of FSP and high thermal conductivity of BMs. For instance, the microstructures of the BM, TMAZ, and SZ of the sample processed at a rotational speed of 450 rpm are shown in Fig. 3. As seen from Fig. 3a, BM had a larger average grain size in which the presence of annealing twins, indicating the annealed condition of the BMs. Figure 3b illustrates the transition area between the BM and SZ i.e. TMAZ. As seen, TMAZ was composed of elongated grains in which the dynamic recrystallization (DRX) is not occurred or is occurred incompletely. This is due to the presence of a sharp gradient of strain, strain rate, and temperature from BM (with the lowest strain and temperature) to the center of the SZ (with the highest strain and temperature). Thus, in TMAZ, due to inadequate stain and temperature, the DRX recrystallization was not completed. Contrarily, in SZ with highest strain and temperature (Fig. 3b), the material undergoes DRX. In addition, formation of equiaxed grains in the SZ show that DRX was completed during FSP. The type of DRX during FSW/P of brasses are studied by some researchers, which indicates that both the continuous DRX (CDRX) and discontinuous DRX (DDRX) happen during the process [15, 16]. CDRX occurs continuously by the gradual transformation of low angle grain boundaries (LAGBs) to high angle grain boundaries (HAGBs). This phenomenon is due to dynamically absorption of dislocations into the LAGBs leading to an increase in their misorientation angle to higher values of 15 degrees. DDRX has two steps of nucleation and growth, which is usually called the classical DRX [9, 17]. In summary, FSP caused transformation of large and equiaxed grains of BMs to fine grains by CDRX and DDRX mechanisms.
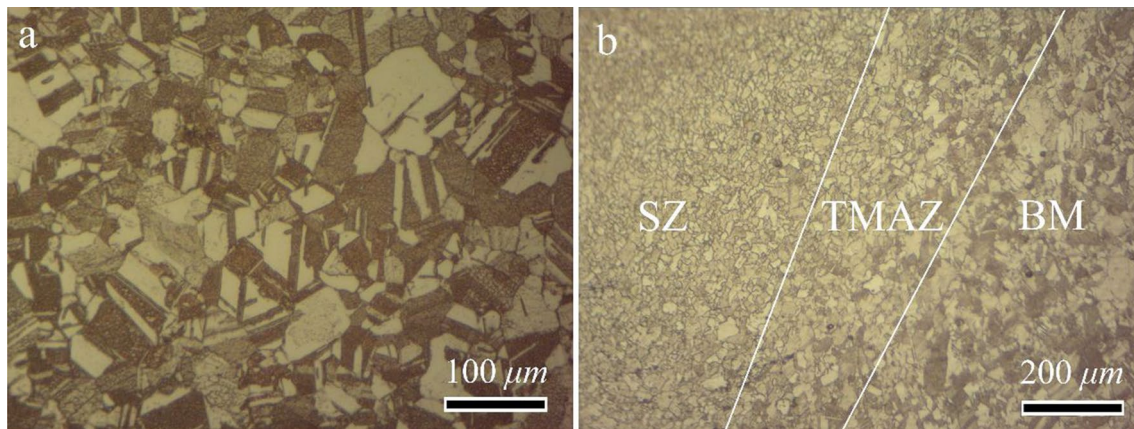
Fig. 3 OM microstructures of **a** BM and **b** transition area between BM and SZ

3.1.1 Effect of rotational speed

The microstructures of SZs for different friction processed samples at rotational speeds of 450, 710, and 1120 rpm are illustrated in Figs. 4, 5 and 6, respectively. Some important points can be extracted from Figs. 4, 5 and 6. All SZs had a complex and bimodal microstructures which can be divided into two main zones. In some zones, the material does not contain Al_2O_3 nano particles, which only have experienced the CDRX and DDRX resulting in new DRX grains. In some zones, the existence of Al_2O_3 nano particles have resulted in finer grain sizes. The effect of Al_2O_3 nano particles on the
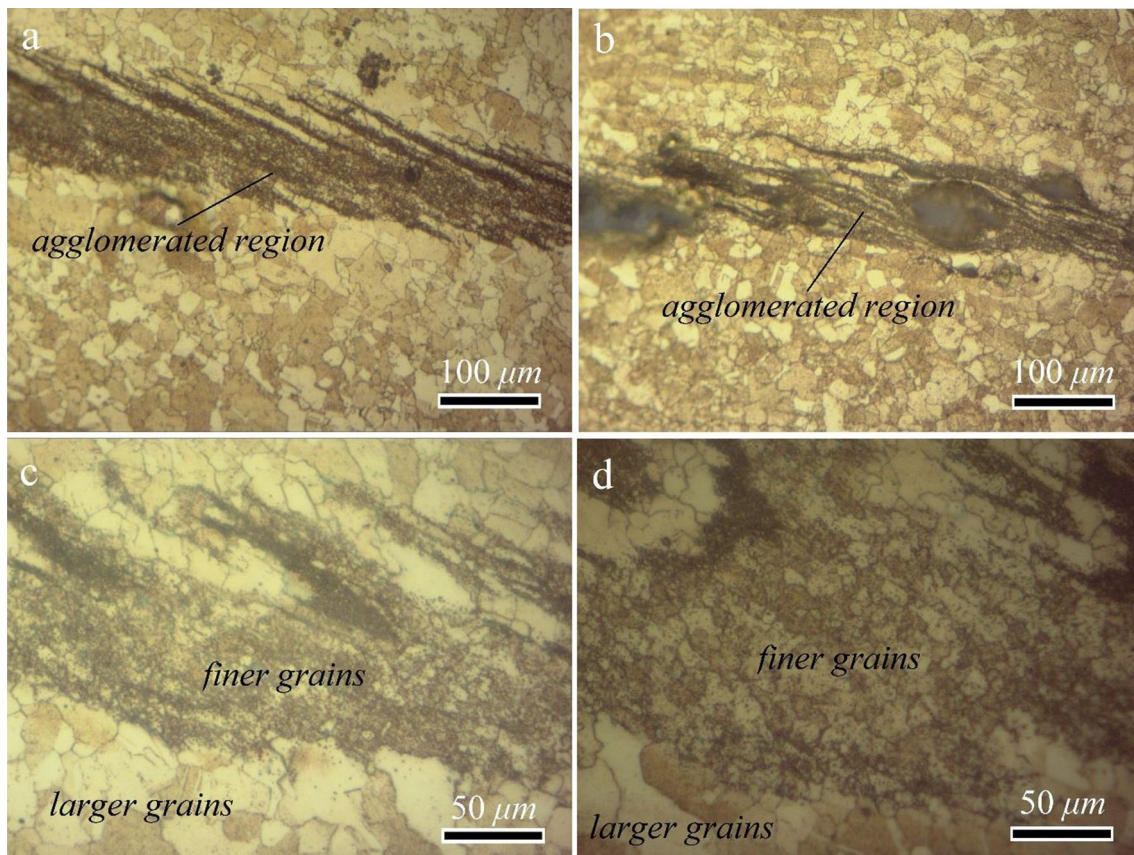

Fig. 4 OM microstructures of SZ in the sample welded at rotational speed of 450 rpm. **c** and **d** are higher magnifications of (**a**) and (**b**), respectively
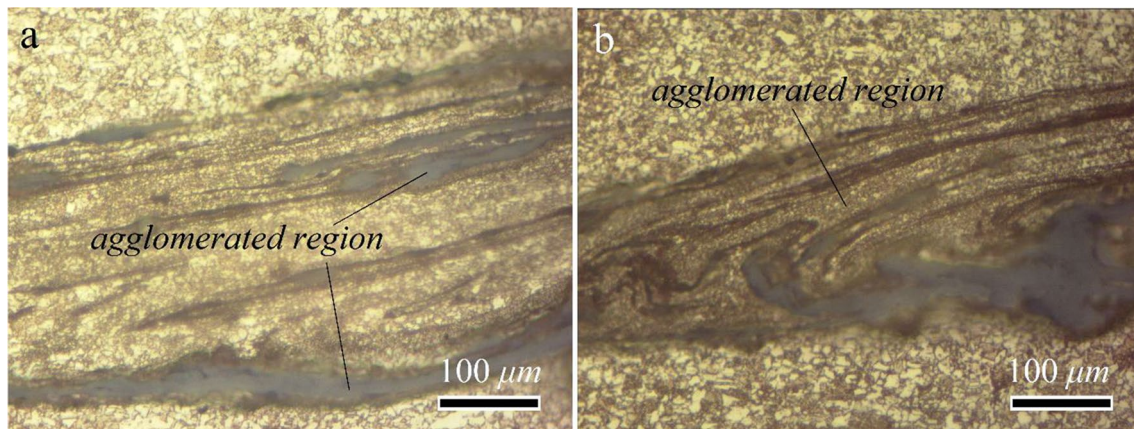
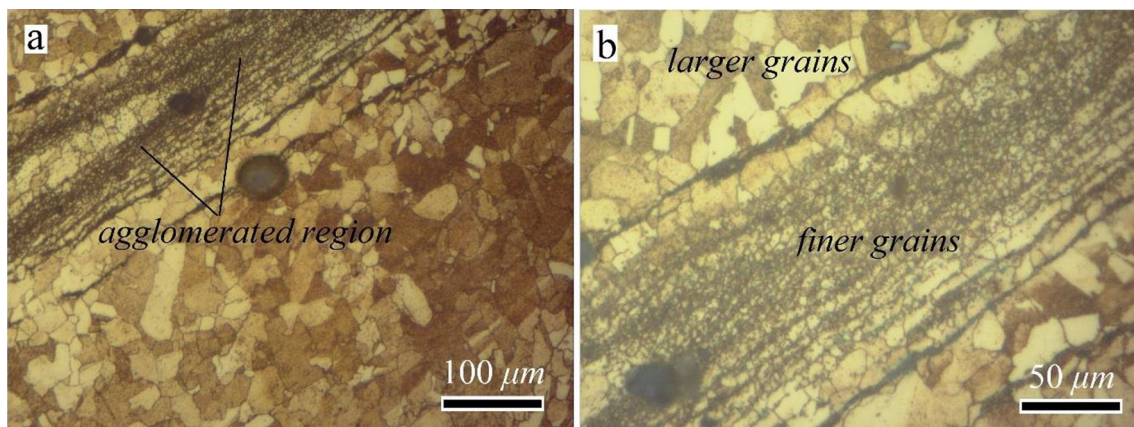**Fig. 5** **a** and **b** OM microstructures of SZ in the sample welded at rotational speed of 710 rpm

Fig. 6 OM microstructures of SZ in the sample welded at rotational speed of 1120 rpm. **c** and **d** are higher magnifications of (**a**, and **b**), respectively

DRX can be explained as follows. Commonly, the secondary non-deformable particles can promote or inhibit DRX depending on their sizes. Large particles (commonly with a diameter larger than 1 μm) act as nucleation sites during DDRX mechanisms, which promote the DRX. On the other hand, the finer particles by preventing grain boundary bulging, inhibit DDRX. In addition, the fine particles can also pin the grain boundaries which reduces their mobility during the growth process [18]. According to this brief explanation, it seems that Al_2O_3 nano particles have pinned the grain boundaries and have postponed growth of DRX grains.

The other important point is better distribution of Al_2O_3 nano particles in the SZ at higher rotational speeds. Figure 4 shows that at 450 rpm, Al_2O_3 nano particles are agglomerated, however, at 710 rpm (Fig. 5) and 1120 rpm (Fig. 6), they are more distributed in the SZs.

Although the Al_2O_3 nano particles were more distributed in the SZ of 1120 rpm, it was not the optimum condition because the tool was damaged at 1120 rpm due to its

severe wear by the Al_2O_3 nano particles as shown in Fig. 7. Therefore, due to disadvantages of 1120 rpm, the optimum rotational speed was 710 rpm, which was used for the rest of the samples to evaluate the effect of number of FSP passes.

3.1.2 Effect of number of passes

Figure 8 shows the SEM images of the sample processed for 1 pass at rotational speed of 710 rpm. As seen, the Al_2O_3 nano particles are completely agglomerated during FSP. The second pass (Fig. 9) caused a reduction in agglomerated areas in the cross section of the processed samples. However, in some regions (Fig. 9), the Al_2O_3 nano particles are still agglomerated. Based on Fig. 9c, in the presence of Al_2O_3 nano particles the grain size is reduced considerably due to its pinning effect on the mobility of grain boundaries just after FSP during the growth step. Figure 10 illustrates the SEM macrograph and microstructure of the SZ in the sample processed by three passes. From Fig. 10a, no agglomeration

Fig. 7 Tools after FSP at rotational speed of 1120 rpm

was observed in the cross section of this sample. The high magnified SEM image of the SZ (Fig. 10b), shows that the Al_2O_3 nano particles are more homogeneously distributed. The SZ (Fig. 10b) consists of two types of grains. The first type includes grains with an average grain size of approximately equal to 3–5 μm. Higher magnification of the SZ (Fig. 11) revealed that these grains contain twin boundaries or Σ3 coincidence site lattice boundaries. It is well documented that these types of twins are formed during grain growth in face centered cubic (FCC) metals [18]. Thus, it can be concluded that in some regions that the concentration of Al_2O_3 nano particles is low, the DRX grains are grown more freely, and hence the twins are formed inside them. The second type belongs to the ultra-fine grained (UFG) regions with grain sizes smaller than 1 μm. In these regions, the Al_2O_3 nano particles inhibit the grain boundary mobility and hence the grain growth is considerably limited during post heating after FSP. In summary, the SZ of 3 passes sample shows a bimodal structure, including UFG grains and 3–5 μm grains.

3.2 Mechanical properties

The ultimate tensile strength (UTS) and elongation of the different tensile samples are summarized in Table 1. Based on the Table 1, an increase in the number of passes leads to synergic increase in strength and elongation. The fracture surface of the tensile samples processed for one and two passes contained agglomerated Al_2O_3 nano particles (Fig. 12), which shows that the fracture initiated from the agglomerated regions. Hence, the elongation of the samples were lower than that of the sample processed for three passes. The increase in UTS from 360 to 398 MPa can be due to the formation of finer grain sizes after the second pass. The superior mechanical properties achieved for the sample processed by three passes (430 MPa UTS and 39% elongation). The origin of this behavior can be explained as follows. Figure 13 illustrates the SEM fractographs in conjunction with EDS analysis of sample processed for three passes. As seen, there were no signs of agglomerated Al_2O_3 nano particles in the fracture surface where the dimples are formed. The presence of dimples confirms that the sample has been fractured under a ductile mode (Fig. 13a). The other point from Fig. 13b–d is the existence of two types of dimples in the fractured surface. Some dimples (Fig. 13c) do not contain Al_2O_3 nano particles indicated by B in Fig. 13b, where some of them (Fig. 13d) have surrounded Al_2O_3 nano particles inside themselves (indicated by A in Fig. 13b). The presence of Al_2O_3 nano particles increases the strain hardening of the sample during tensile test, because they act as dislocation storage sites. On the other hand, Al_2O_3 nano particles can act as barriers to dislocation movement, which results in higher strength. In addition, it is well documented that the formation of bimodal structures causes synergic increase in strength and elongation [19]. Moreover, the existence of UFG structure leads to increase in strength according to the grain boundary strengthening mechanism ($\Delta\sigma_{GR}$) or Hall–Petch equation. The increase in yield strength in the produced composites can be expressed as follows [20]:

$$\Delta\sigma_{GR} = K\left(d_c^{-1/2} + d_a^{-1/2}\right) \tag{1}$$

In Eq. 1, K is the Hall–Petch constant, d_c and d_a are the average grain size of composite and matrix, respectively.
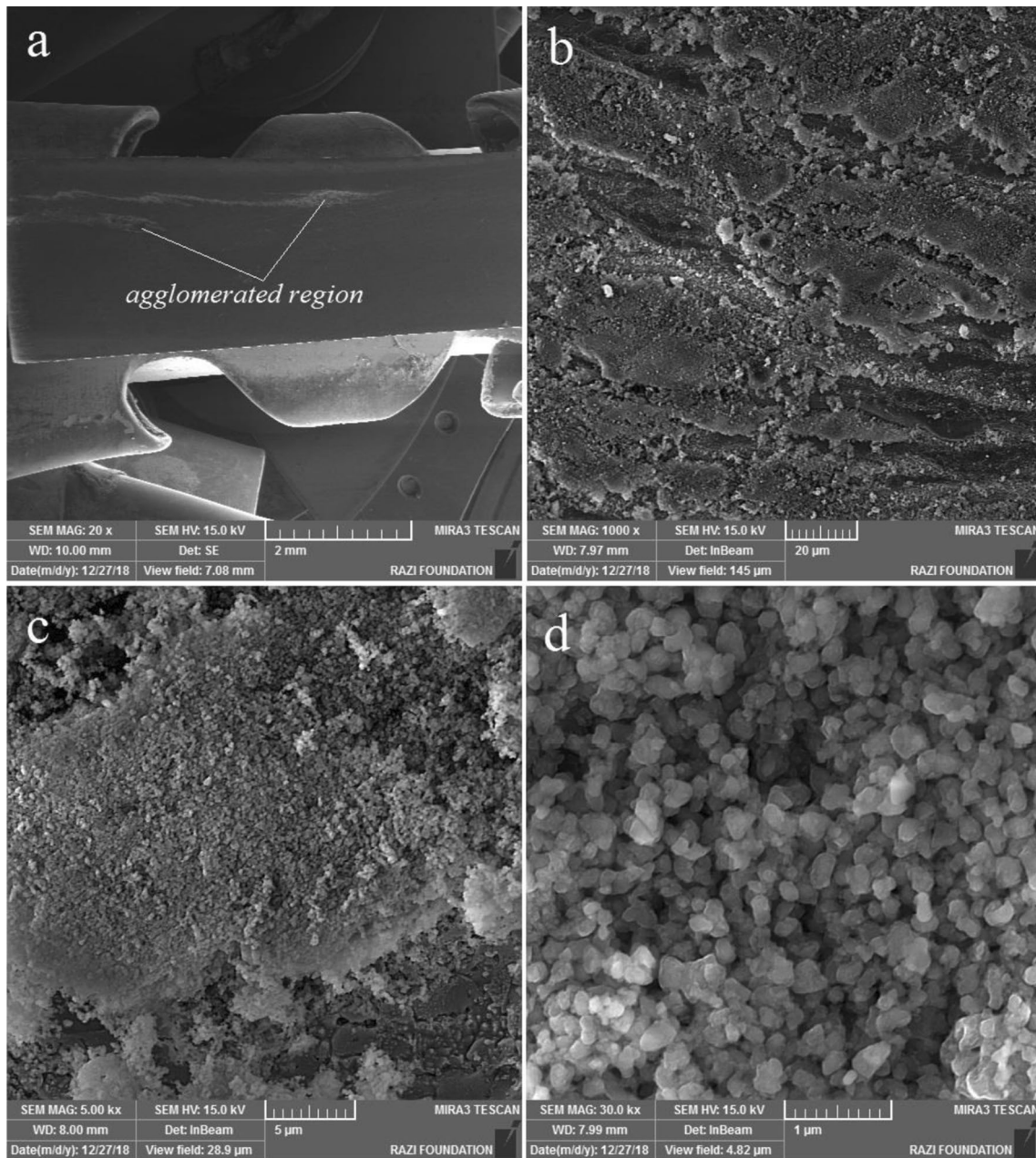
Fig. 8 Friction stir processed sample at rotational speed of 710 rpm and for one pass. SEM images of **a** macrostructure, **b–d** higher magnification of agglomerated Al_2O_3 zone in (**a**)

In addition to the mentioned mechanisms, the other mechanisms such as dislocation strengthening and effect of texture are also probable mechanism according to the literature [21]. In the load bearing effect ($\Delta\sigma_{LB}$), high density of dislocations around the reinforcements results in large plastic strain fields, and hence large amount of applied stress is needed to continue the deformation. $\Delta\sigma_{LB}$ can be formulated as follows [22]:

$$\Delta\sigma_{LB} = VF_{RE}(S/A)\left(\tau_a/2\right) + \sigma_a VF_a \qquad (2)$$

In Eq. 2, VF_{RE} and VF_a are volume fraction of reinforcements and matrix, respectively. σ_a and τ_a are yield and shear strengths of matrix. S and A refer to the interfacial and cross sectional area of reinforcements. Furthermore, the difference between thermal coefficient of matrix and reinforcements cause to production of dislocations during
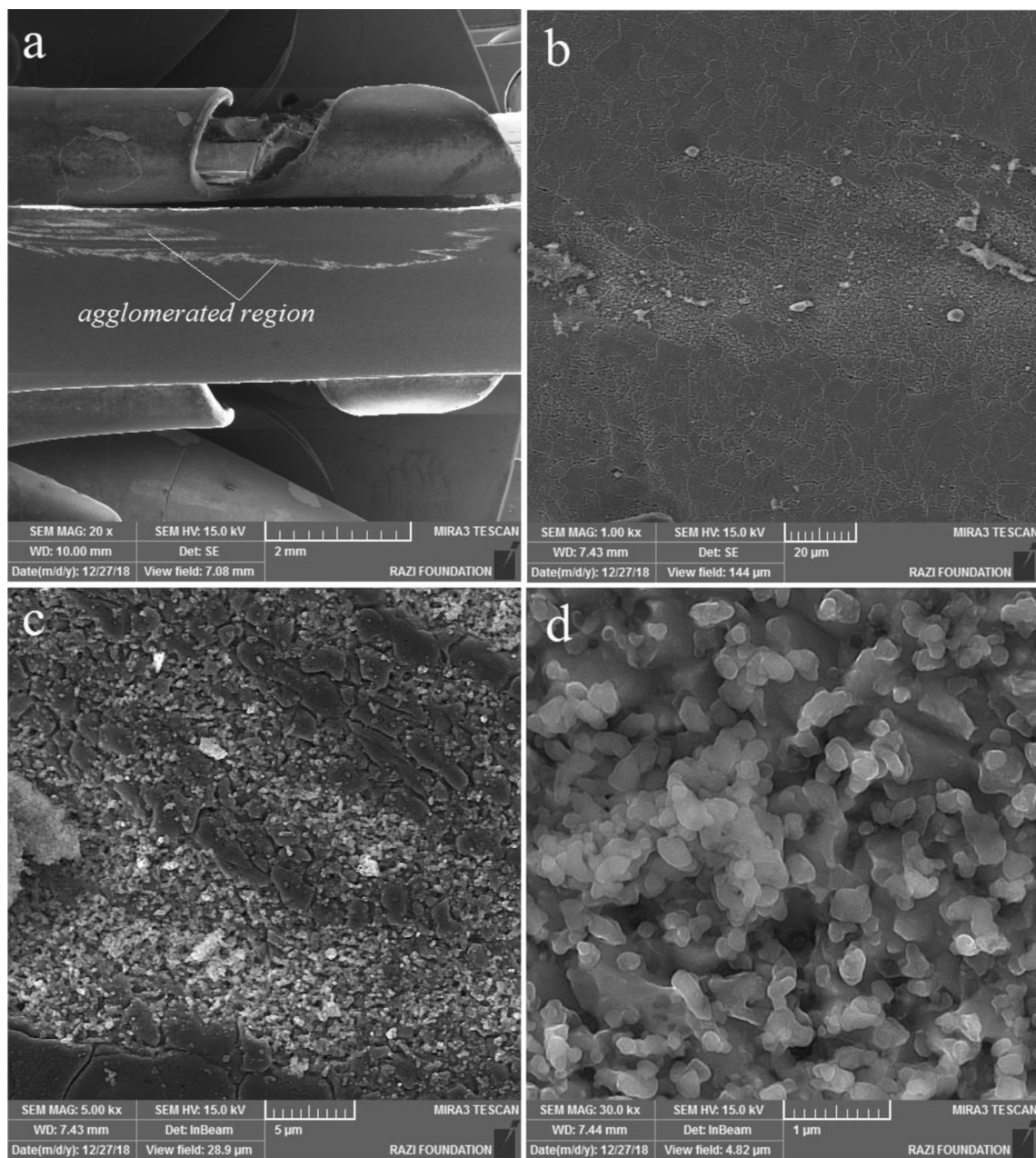
Fig. 9 Friction stir processed sample at rotational speed of 710 rpm and for two passes. SEM images of **a** macrostructure, **b–d** higher magnification of agglomerated Al_2O_3 zone in (**a**)

cooling cycle of process, which is called usually thermal mismatch mechanism ($\Delta\sigma_{TM}$). Thermal mismatch mechanism is one of the main mechanisms causing higher yield strength in composites in which the generated geometrically necessary dislocations results in work hardening [23]. Moreover, the Orowan mechanism ($\Delta\sigma_{OR}$) can also contribute in strengthening of composites. In this

mechanism, interaction of moving dislocations with reinforcements causes bending of dislocations and producing back stresses, which hinders migration of dislocations [24].

In summary, the strengthening mechanism involved in superior strength of sample processed by three passes are grain boundary strengthening, secondary phase effect,
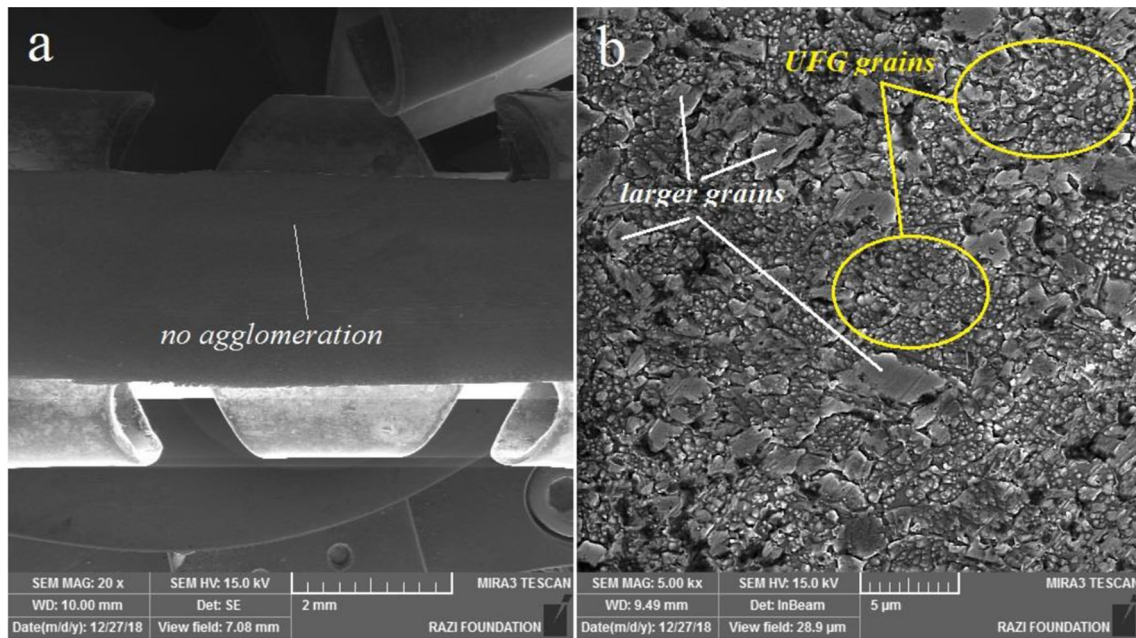
Fig. 10 Friction stir processed sample at rotational speed of 710 rpm and for three passes. SEM images of **a** macrostructure, **b** higher magnification of microstructure in (**a**)
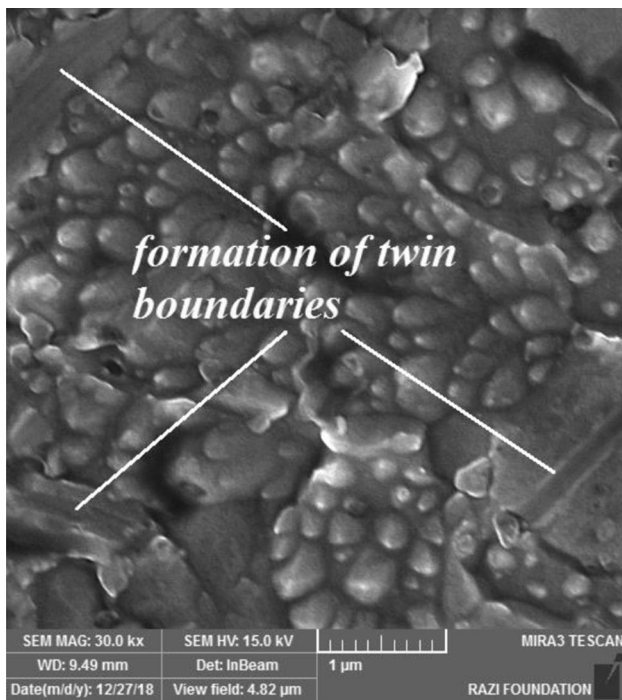

Fig. 11 High magnified SEM image of friction stir processed sample at rotational speed of 710 rpm and for one pass. A bimodal grain size is formed in the SZ

Table 1 UTS and elongation of the BM and different tensile samples

Sample	Ultimate tensile strength (UTS) (MPa)	Elongation (%)
BM	304	54
710 rpm—1 pass	360	28
710 rpm—2 pass	398	34
710 rpm—3 pass	430	39

dislocation strengthening, and texture effect. On the other hand, the reason for higher elongation are the effect of nanoparticles and bimodal structures on strain hardening effect.

4 Conclusion

Brass-Al_2O_3 surface nano composites were produced using FSP at different conditions, and the following conclusions can be summarized:

1) At a constant traverse speed of 100 mm/min, an optimum condition of 710 rpm should be used. At lower rotational speeds, i.e. 450 rpm, Al_2O_3 nano particles are agglomerated within the SZ. Higher rotational speeds,
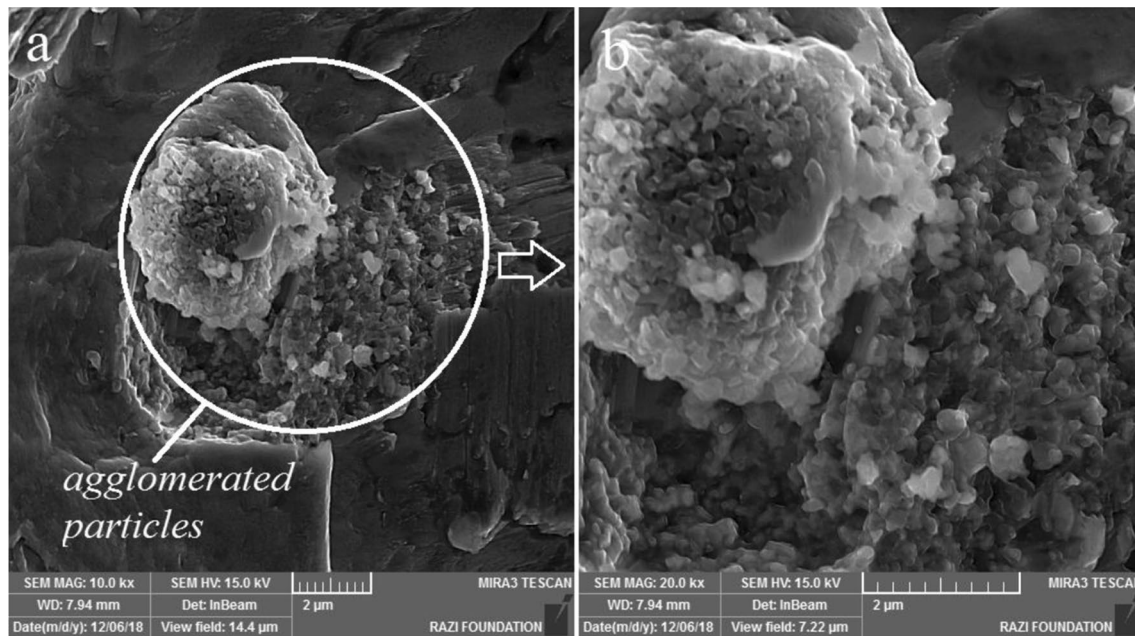
Fig. 12 a SEM image of fractured surface of friction stir processed sample at rotational speed of 710 rpm and for two passes. **b** Higher magnification of (**a**)

i.e. 1120 rpm, cause tool wear by ceramic nano particles during FSP.

2) Multi-pass FSP at optimum rotational speed (710 rpm) is very useful to distribute the Al_2O_3 nano particles, uniformly. For this aim, three passes sample is selected as the optimum condition. One and two passes do not eliminate the agglomerated particles within the SZ.

3) Al_2O_3 nano particles pin the grain boundaries of DRX grains, and hence inhibit their growth after tool pass during FSW. Therefore, at the zones with the presence of Al_2O_3 nano particles, the average grain size is reduced, considerably, which caused a bimodal structure.

4) At the optimum condition, i.e. 710 rpm and three passes, the SZ shows an interesting bimodal structure, including larger grains (3–5 μm) and UFG grains (< 1 μm).

5) Multi-pass FSP leads to synergic increase of UTS and elongation. Three passes results in superior tensile properties such as UTS of 430 MPa and elongation of 39%. The strengthening mechanisms of effects of grain boundaries and secondary phase cause higher UTS values. The agglomerated Al_2O_3 nano particles in the fractured surface of tensile samples are the main reason of lower elongation in one and two passes FSPed materials. Where, in three passes FSP, the fracture surface showed a ductile behavior containing two types of dimples with and without Al_2O_3 nano particles. The presence of Al_2O_3 nano particles inside the dimples demonstrates their effect on the stain hardening during tensile test, and hence they cause higher elongation.
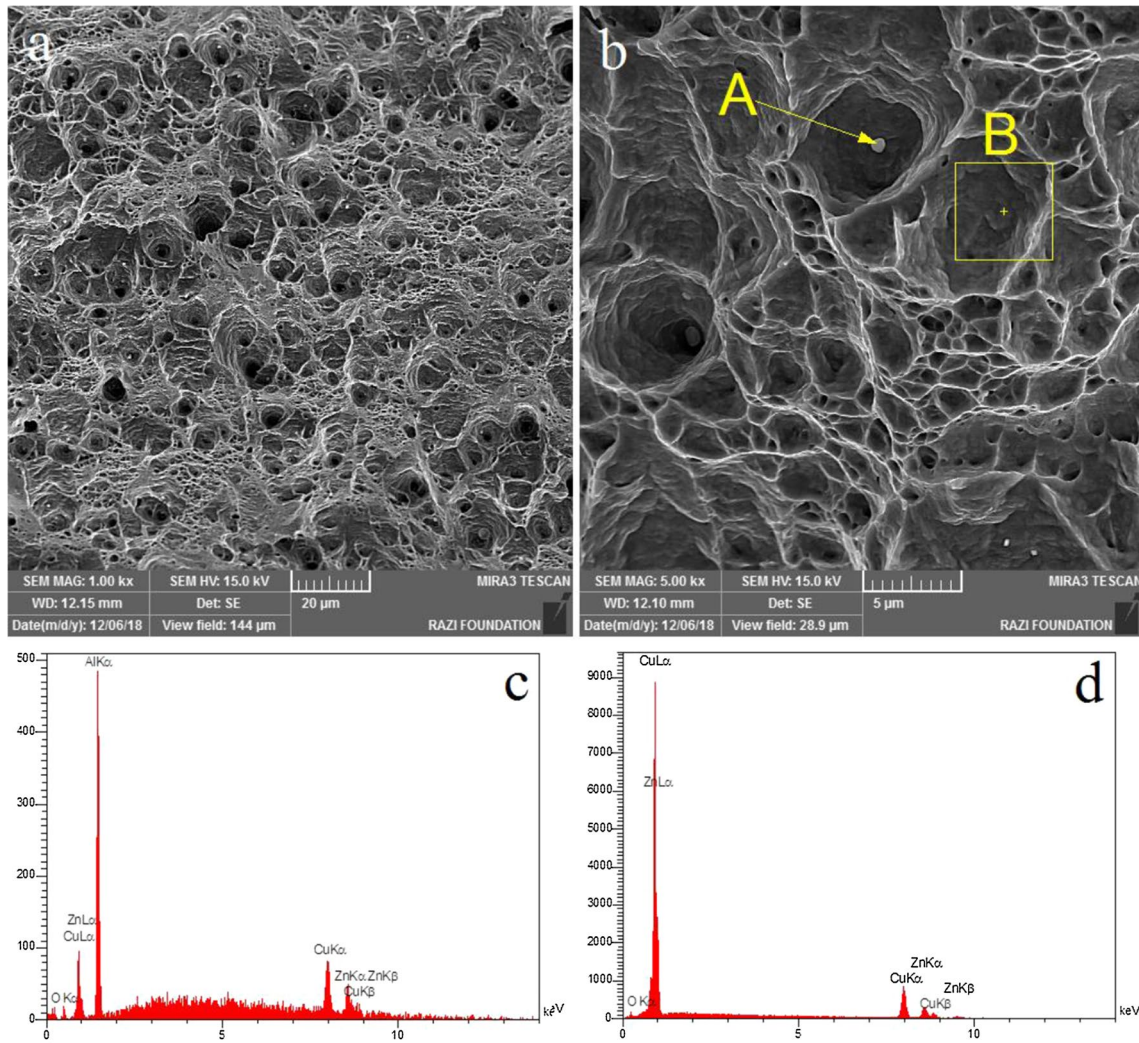
Fig. 13 **a** SEM image of fractured surface of friction stir processed sample at rotational speed of 710 rpm and for three passes. **b** Higher magnification of (**a**). (**c** and **d**) EDS analysis of points A, and B in (**b**), respectively

References

1. Ibrahim IA, Mohamed FA, Lavernia EJ. Particulate reinforced metal matrix composites—a review. J Mater Sci. 1991;26(5):1137–56.
2. Fecht HJ, Ivanisenko Y. 4—Nanostructured materials and composites prepared by solid state processing. In: Koch CC, editor. Nanostructured materials (second edition). Norwich, NY: William Andrew Publishing; 2007. p. 119–172.
3. Sharma V, Prakash U, Kumar BVM. Surface composites by friction stir processing: a review. J Mater Process Technol. 2015;224:117–34.
4. Ajay Kumar P, Madhu HC, Pariyar A, Perugu CS, Kailas SV, Garg U, Rohatgi P. Friction stir processing of squeeze cast A356 with surface compacted graphene nanoplatelets (GNPs) for the synthesis of metal matrix composites. Mater Sci Eng: A. 2020;769:138517.
5. Yao X, Feng X, Shen Y, Li B, Zhang J, Xu H, Kuang B. Microstructure feature of friction stir processed ductile cast iron. Mater Des (1980–2015). 2015;65:847–54.
6. Lee CJ, Huang JC, Hsieh PJ. Mg based nano-composites fabricated by friction stir processing. Scripta Mater. 2006;54(7):1415–20.
7. Ahmadkhaniha D, Heydarzadeh Sohi M, Salehi A, Tahavvori R. Formations of AZ91/Al2O3 nano-composite layer by friction stir processing. J Magnes Alloys. 2016;4(4):314–8.
8. Du Z, Tan MJ, Guo JF, Bi G, Wei J. Fabrication of a new Al-Al2O3-CNTs composite using friction stir processing (FSP). Mater Sci Eng, A. 2016;667:125–31.
9. Heidarzadeh A, Pouraliakbar H, Mahdavi S, Jandaghi MR. Ceramic nanoparticles addition in pure copper plate: FSP approach, microstructure evolution and texture study using EBSD. Ceram Int. 2018;44(3):3128–33.
10. Shafiei-Zarghani A, Kashani-Bozorg SF, Zarei-Hanzaki A. Microstructures and mechanical properties of Al/Al2O3 surface nano-composite layer produced by friction stir processing. Mater Sci Eng A. 2009;500(1–2):84–91.

11. Khodabakhshi F, Arab SM, Švec P, Gerlich AP. Fabrication of a new Al-Mg/graphene nanocomposite by multi-pass friction-stir processing: dispersion, microstructure, stability, and strengthening. Mater Charact. 2017;132:92–107.

12. Huang Y, Xie Y, Meng X, Lv Z, Cao J. Numerical design of high depth-to-width ratio friction stir welding. J Mater Process Technol. 2018;252:233–41.

13. Su H, Wu CS, Pittner A, Rethmeier M. Thermal energy generation and distribution in friction stir welding of aluminum alloys. Energy. 2014;77:720–31.

14. Huang Y, Xie Y, Meng X, Li J, Zhou L. Joint formation mechanism of high depth-to-width ratio friction stir welding. J Mater Sci Technol. 2019;35(7):1261–9.

15. Mironov S, Inagaki K, Sato Y, Kokawa H. Development of grain structure during friction-stir welding of Cu–30Zn brass. Phil Mag. 2014;94(27):3137–48.

16. Heidarzadeh A, Saeid T, Klemm V. Microstructure, texture, and mechanical properties of friction stir welded commercial brass alloy. Mater Charact. 2016;119:84–91.

17. Sakai T, Belyakov A, Kaibyshev R, Miura H, Jonas JJ. Dynamic and post-dynamic recrystallization under hot, cold and severe plastic deformation conditions. Prog Mater Sci. 2014;60:130–207.

18. Humphreys FJ, Hatherly M. Recrystallization and related annealing phenomena. Elsevier; 2012.

19. Arora H, Ayyagari A, Saini J, Selvam K, Riyadh S, Pole M, Grewal H, Mukherjee S. High tensile ductility and strength in dual-phase bimodal steel through stationary friction stir processing. Sci Rep. 2019;9(1):1–6.

20. Mokdad F, Chen DL, Liu ZY, Xiao BL, Ni DR, Ma ZY. Deformation and strengthening mechanisms of a carbon nanotube reinforced aluminum composite. Carbon. 2016;104:64–77.

21. Heidarzadeh A. Tensile behavior, microstructure, and substructure of the friction stir welded 70/30 brass joints: RSM EBSD, and TEM study. Arch Civil Mech Eng. 2019;19(1):137–46.

22. Rashad M, Pan F, Asif M, Tang A. Powder metallurgy of Mg–1%Al–1%Sn alloy reinforced with low content of graphene nanoplatelets (GNPs). J Ind Eng Chem. 2014;20(6):4250–5.

23. Magnus C, Sharp J, Ma L, Rainforth WM. Ramification of thermal expansion mismatch and phase transformation in TiC-particulate/SiC-matrix ceramic composite. Ceram Int. 2020;46(12):20488–95.

24. Szajewski BA, Crone JC, Knap J. Analytic model for the Orowan dislocation-precipitate bypass mechanism. Materialia. 2020;11:100671.